Bull. Chem. Soc. Ethiop. **2023**, 37(1), 211-229.
DOI: https://dx.doi.org/10.4314/bcse.v37i1.17

ISSN 1011-3924
Printed in Ethiopia
Online ISSN 1726-801X

EFFICIENT ADSORPTION OF RHODAMINE B USING A COMPOSITE OF Fe_3O_4@ZIF-8: SYNTHESIS, CHARACTERIZATION, MODELING ANALYSIS, STATISTICAL PHYSICS AND MECHANISM OF INTERACTION

Ghaferah H. Al-Hazmi[1], Abdel Majid A. Adam[2], Mohamed G. El-Desouky[3*], Ashraf A. El-Bindary[4*], Amnah M. Alsuhaibani[5] and Moamen S. Refat[2]

[1]Department of Chemistry, College of Science, Princess Nourah bint Abdulrahman University, P.O. Box 84428, Riyadh 11671, Saudi Arabia
[2]Department of Chemistry, College of Science, Taif University, P.O. Box 11099, Taif 21944, Saudi Arabia
[3]Egyptian Propylene and Polypropylene Company, Port Said 42511, Egypt
[4]Chemistry Department, Faculty of Science, Damietta University, Damietta 34517, Egypt
[5]Department of Physical Sport Science, College of Education, Princess Nourah bint Abdulrahman University, P.O. Box 84428, Riyadh 11671, Saudi Arabia

(Received July 15, 2022; Revised August 30, 2022; Accepted September 9, 2022)

ABSTRACT. The utilization of a metal organic framework (ZIF-8) modified by Fe_3O_4 nanoparticles was used to accomplish adsorption of Rhodamine B (RB) from aqueous solutions. SEM, XRD, IR, and BET analyses were all used to characterize the composite (Fe_3O_4@ZIF-8). The surface area of this adsorbent was 478.4 m^2/g. X-Ray diffraction spectroscopy was used to detect surface modification utilizing electron microscopy (SEM) scanning with 48 nm in diameter average particle size according to a statistical physics method. Fe_3O_4@ZIF-8 appears to have dispersive interactions and pore characteristics, according to quantum chemistry simulations. On the adsorption of RB, the influences of contact time, adsorbent quantity, dye concentration, and temperature were studied. The Langmuir and Freundlich adsorption isotherm models were used to study the adsorption isotherms. Anticipated overall adsorption potential was 647.5 mg/g, with a zero-charge point (pH_{PZC}) of 4.3. The adsorption isotherm was fitted using Langmuir whereas pseudo second order was used to match the kinetics. Energy of adsorption (E_a) is 28.7 kJ/mol, indicating a chemisorption phase. The adsorption process is endothermic and unpredictable, according to thermodynamic experiments. It was also looked into using ethanol as a solvent in the desorption of deposited cationic dye.

KEY WORDS: Fe_3O_4@ZIF-8, Rhodamine B, Adsorption models, Thermodynamics

INTRODUCTION

Dyes are used to color final goods in textiles, paper, plastics, cosmetics, and leather, to name a few. The emission of colored wastewater from these industries could be environmentally hazardous, and also pose a risk of bioaccumulation, which could eventually damage humans via the food chain. Colors are toxic and restrict light penetration; therefore wastewater with even a little number of dyes can have a substantial influence on aquatic species [1]. Due to the obvious brightly colored waste they generate, dyeing companies are a major pollutant in the world [2]. The three types of dyes are cationic (basic dyes), anionic (acid dyes), and non-ionic (dispersed dyes). It is now crucial from an environmental standpoint to treat wastewaters to eliminate colour. In aqueous solution, cationic dyes have a net positive charge due to their protonated amine or sulfur-containing groups, whereas anionic dyes have a net negative charge due to their sulphonate groups. Therefore, it is essential to cleanse these discharge pigments before dispersing them in water. Additionally, because of their aromatic structure, they are more stable and more resistant to degradation. Dyes are impervious to sunny, other contaminants, oxidizing mediators, and due

*Corresponding author. E-mail: ch.moh.gamal@gmail.com

to their chemical structure, they are physiologically inert proving them impossible to collect once release into the water habitats [3]. The contamination of receiving streams by this colored water has the ability to ruin aquatic life [4, 5].

Ultrafiltration, coagulation, oxidation, ozonation, reverse osmosis, sedimentation, flotation, and precipitation are a few of the modern methods utilised to filter water based on cost issues. Procedures for handling textile colours during treating wastewater can be difficult. The demonstrated success of converting waste into stable chemicals using adsorption has led to its increased popularity over the conventional techniques mentioned above in latest years [6].

Metal organic frameworks (MOFs) are pores crystalline frameworks made up of organic ligands with metal ions (or clusters). MOFs have piqued the curiosity of scientists all over the world, and they've been used in a variety of applications. Gas separation and recycling, catalysis, adsorbents, and energy storage are some of the technologies used. MOFs are increasingly being used for the adsorption and elimination of numerous harmful compounds from watery solutions, with both inorganic and organic contaminants as targets [7]. Adsorption between contaminants and MOFs is influenced by hydrophilic groups, electrical amplification, and interactions. They have substantial porosities, a very diverse surface, and intense electrostatic attraction. According to prior reports, MOFs are useful for capturing certain dyes in aquatic systems.

ZIF-8 are crystalline microporous materials with remarkable thermal and chemical persistence that have piqued interest for dye adsorption to elevated amounts of permanence in the case of MOFs [8, 9]. The ZIF-8 network is made up of Zn^{2+} atoms prepared as [ZnN_4] tetrahedrons with 2-methylimidazolate linker N atoms. Due to the obvious ease of magnetic separation, which allows the adsorbed colors to be retrieved, this technique is more effective than reaction mixtures, nanofiltration, or centrifugation over a membrane. Saturation magnetization nanoparticles are normally non-magnetic, but they can become magnetized quickly in the influence of environmental magnetic fields [10, 11]. The nanoparticles can be easily cleaned from the reaction media using an external magnet or centrifugation, removing the requirement for filtration. Magnetic particles are also chemically stable, and in some chemical processes, they can be referred to be inert. Finally, nanoparticles are a low-cost and promising magnetic insulating material for commercial processes [12-14]. Because they belong to a unique class of crystalline materials with intriguing prospective uses, porous magnetite nanoparticles (Fe_3O_4) [15]. Recently, there has been a lot of interest in the manufacturing of magnetite that has been scaled down to the nanometer level [16, 17].

In this search, synthesized and characterized Fe_3O_4@ZIF-8 nanocomposite in a novel way that gives highly surface area of 478.4 m^2/g and effective removal of RB from wastewater 1.46 mmol/g. as the nanocomposite has magnetic properties so it's easy to remove RB@Fe_3O_4@ZIF-8 instead of using a centrifuge. The effects of initial dye concentration, solution pH, Fe_3O_4@ZIF-8 dose, contact time, and the effect of temperatures and time on the adsorption cycle were studied. The results were analyzed using the equilibrium adsorption data, isotherm, and kinetic models from the experiments. And on the other hand the reusability of these nanocomposites has been used about six times.

EXPERIMENTAL

Chemicals

Without additional purification procedures, chemicals were used as obtained. Ammonium ferrous sulfate ($(NH_4)_2(FeSO_4)_2{\cdot}6H_2O$), 99%, Tianjin Kemiou Chemical Reagent, China), 2-methylimidazole (Hmim) (Sinopharm chemical reagent Co. Ltd., China), ferric chloride ($FeCl_3{\cdot}6H_2O$), anhydrous ethanol (99.7%, Sinopharm chemical reagent Co. Ltd., China), and Rhodamine B (Merck KGaA, 64271 Darmstadt, Germany) were used.

Synthesis of porous magnetite nanoparticles Fe_3O_4 and its composite Fe_3O_4@ZIF-8

Porous magnetite nanoparticles Fe_3O_4 and its composite of magnetite Fe_3O_4@ZIF-8 were prepared previously [18].

Characterization of Fe_3O_4@ZIF-8

All the apparatus used are discussed previously [5, 12].

Experiments on batch adsorption

An adequate amount of RB can be prepared by dispersing it in bidistilled water and can test limitations as pH (2-12) and a standard solution ($1x10^{-3}$ mol/L) of (RB). Fe_3O_4@ZIF-8 dosage to be (0.01 to 0.10 g) in 25 mL and adsorbents temperature (25-55 °C) on RB aqueous solution adsorption examined in detail. Separation was achieved by centrifuging the adsorbent at 4000 rpm (Figure 1) [19]. The percentage of colorants for RB was estimated using UV-Vis at 543 nm. The dye removal rate (R) was calculated using Eq. (1):

$$\%R = \frac{(C_0 - C_t)}{C_0}\ x\ 100 \quad (1)$$

However, the adsorption capacity is calculated using the equation of weight equilibrium (q_e, mmol/g) (Eq. 2) [20]:

$$\mathbf{q_e} = \frac{(\boldsymbol{C_0 - C_e})\boldsymbol{V}}{\boldsymbol{M}} \quad (2)$$

The amount of sorbet dye per sorbent unit weight is predicted to be t (q_t, mmol/g) using the equation for mass balance. Following is the result, taking into account the reduction in value is increased (Eq. 3):

$$\boldsymbol{q_{(t)}} = \sum_{\boldsymbol{i=1}}^{\boldsymbol{n}} \frac{[\boldsymbol{C(t)_{(i-1)} - C(t)_{(i)} V(t)_{(i-1)}}]}{\boldsymbol{M}} \quad (3)$$

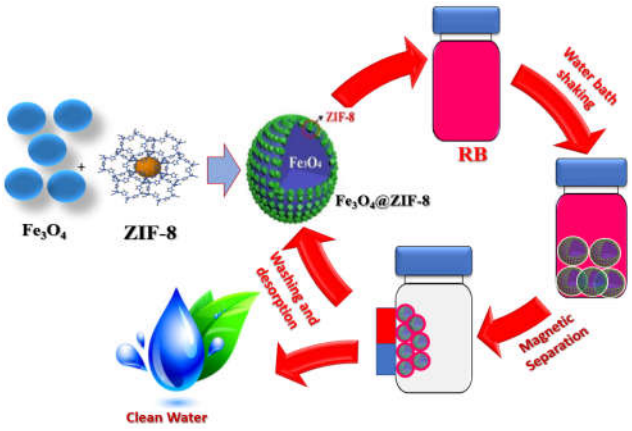

Figure 1. The schematic diagram for RB adsorption on Fe_3O_4@ZIF-8.

Statistical and physical simulation

In statistical physics-based computations of adsorption systems, would use a large canonical ensemble provides for physical interpretations based on experimental results. Some assumptions have been made to achieve this. First, the statistical physics procedure used to calculate the form of an observation isotherm, the much more successful adsorption isotherm equation is influenced by a variety of factors. The IUPAC categorization system was used to define the type of adsorption isotherm. Therefore, the first step is to select the most appropriate model from the range of options. Modeling of monolayer adsorption combined through inert gas (MMIG) and model of monolayer adsorption joined through real gas (MMARG) were utilized for the monolayer adsorption study (MMRG). The MMRG model evaluates the likelihood of adsorbate molecules interacting on the sorbent surface. According to the MMIG model, no such interactions will occur. When considering how lateral interactions affect the adsorption mechanism, this idea is especially important. Both theories suggest that the RB can, at any given energy level, be multi-anchored or multi-molecularly adsorbed on the Fe_3O_4@ZIF-8. In other words, both models permit the determination of crucial steric and energy components in the adsorbent.

Adsorption isotherm models like Langmuir, but on the other hand, explain the process of adsorption on an adsorbent's surface adsorption in a monolayer on completely heterogeneous surfaces with a fixed number of indiscernible sites and restricted interaction between adsorbate species. Because of the varied affinity of the adsorption sites, adsorption on a heterogeneous surface is the subject of Freundlich's research. The strongest active sites are filled initially, and as the degree of occupation rises, the binding strength diminishes. Pressurized vapors, as suggested by Dubbin-Radushkevich, are absorbed by micropore solids during the regeneration phase [21].

To obtain correct model expressions, the steps listed below should be followed. Develop a function called grand canonical partitioning that is necessary (Eq. 4):

$$Z_{gc} = \sum_{N_i} e^{-\beta(-\varepsilon_i - \mu)N_i} \tag{4}$$

Calculate the number of N_m receptors that have occupied similar locations (Eq. 5):

$$N_0 = \frac{1}{\beta} \frac{\sigma \ln(Z_{gc})^{Nm}}{\sigma \mu} \tag{5}$$

Calculate the adsorbed amount formula, n (Eq. 6):

$$Q_m = n \text{ X No} \tag{6}$$

where μ is the thermodynamic potential of the adsorption mechanism, $(-\varepsilon_i)$ and N_i the adsorption strength and the amount of activated particular receptors I, $\beta = 1/K_BT$, where T is the temp of the operation, and K_B Boltzmann constant. Finally, n is the quantity of compound(s) absorbed per site or the proportion of Table 1.

RESULTS AND DISCUSSION

X-ray diffraction

X-Ray diffraction (XRD) of powders study further validated the encapsulation of Fe_3O_4 in ZIF-8 (Figure 2). Fe_3O_4@ZIF-8 particles have a comparable XRD pattern to ZIF-8, implying that the ZIF-8 crystals' sodality structure continued constant after the Fe_3O_4 particles were created. There

were no more peaks that indicated the high purity of the final Fe_3O_4@ZIF-8 particles, with the exclusion of three peaks at 2θ = 33.47, 35.77, and 43.6° conforming to the (220), (311), and (400) magnetite crystal surfaces (JCPDS No. 19-0629) [26].

The Fe_3O_4@ZIF-8 crystal system for investigation displayed a crystal structure that is monoclinic through planetary group P_{21}, the lattice constraints, were determined through fool proof and check cell software; a = 18.2790 Å, 2.7490 Å, c = 17.2500 Å, α = 90.00°, β = 103.19 and γ = 90.0°.

Table 1. The four isothermal models are represented analytically.

Model isotherm	Amount of expression absorbed	Equation	Reference
MMIG	$Q_a = \frac{nN_m}{1+(\frac{W}{c})}$	(7)	[22]
MMRG	$Q_a = \frac{nN_m}{1+(W\frac{1-bC}{C}\, e^{2\beta C} e^{-}\frac{bC}{1-bC})^n}$	(8)	[23]
Double-Layer Model	$Q_a = Q_S*(\frac{X_1+2X_2^2}{1+X_1+2X_2^2})$	(9)	[24]
Multi-Layer Model	$Q_a = Q_S * \frac{X_1+X_1X_2\left(1-2X_2^L-LX_2^{L+1}+\frac{X_2(1-X_2^L}{1-X_2}\right)}{(1-X_1)(1-X_2)+X_1X_2\,(1-X_2^L)}$	(10)	[25]

Crystallite size and strain determination

Scherrer method

A polycrystalline configuration of the ZIF-8, Fe_3O_4, and Fe_3O_4@ZIF-8 nanoparticles was recommended since of the peak locations and strength proportions. The size of crystallite Fe_3O_4@ZIF-8 nanoparticles was determined by the incomes of the Scherrer formulation. The amended instrumental broadening βhkl conforming to peak Fe_3O_4@ZIF-8 diffraction was assessed through the calculation (Eq. 11):

$$\beta_{hkl} = [\,(\beta_{hkl})^2_{measured} - \beta^2_{instrumental}]^{1/2} \quad (11)$$

It is generally known that the Scherrer method only gives the crystallite size's lowest bound. Using the Scherrer formula, the diameter of crystalline nanoparticles is determined (Eq. 12):

$$D = \frac{K\lambda}{\beta \cos\theta} \quad (12)$$

where λ is the wavelength of X-ray (1.54 Å), β is reduced by the horizontal width of the maximum at half its greatest amplitude, which accounts for instrumental extension (maximum width by half-width), K is the Scherrer continuous (0.9 Å). Fe_3O_4@ZIF-8 crystallite size determined at in height strength peak at high-intensity peak, was 44.9 nm for Fe_3O_4@ZIF-8 (Figure 2).

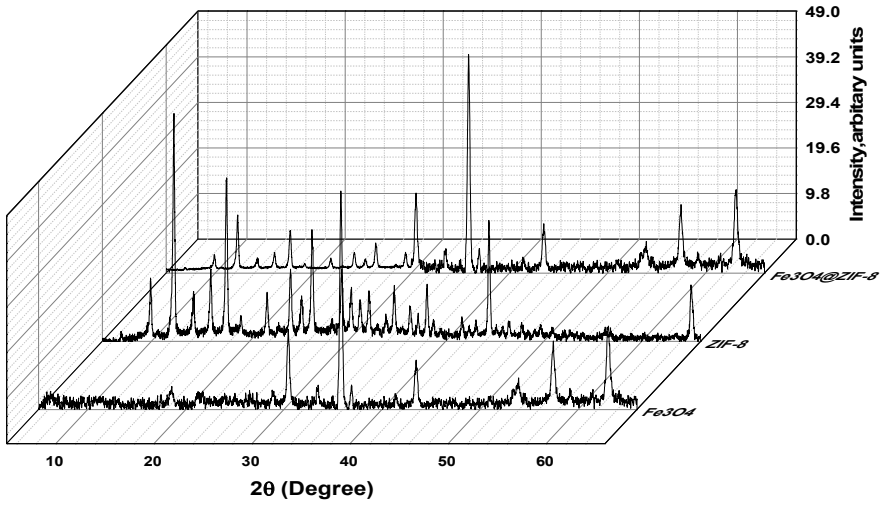

Figure 2. XRD forms of ZIF-8, Fe_3O_4 and Fe_3O_4@ZIF-8.

Williamson–Hall (W–H) method

In several instances, factors other than crystallite size, like lattice strain and imperfections, may also affect X-ray diffraction patterns. The W-H evaluation, a condensed version of the integral breath approach, distinguishes between the maximum of deformation caused by strain and so by armature size while taking into account the widening of the maximum as a factor of 2 θ. As shown in (Eq. 13), each individual can contribute to the peak broadening of a Bragg reflected line:

$$\beta_{hkl} = \beta_S + \beta_D \quad (13)$$

where β_{hkl} signifies the occupied breadth at half maximum (FWHM) of a radiant highest, and β_s β_D are the breadth due to the size–strain, individually. In the W–H relative, it is expected that the straining is unvarying through the crystallographic way, which is assumed through β_{hkl} (Eq. 14):

$$\beta_{hkl} = \frac{K\lambda}{D\cos\theta} + 4\varepsilon \tan\theta \quad (14)$$

Rearranging Eq. 14 gives Eq. 15:

$$\beta_{hkl}\cos\theta = \frac{K\lambda}{D} + 4\varepsilon \tan\theta \quad (15)$$

At this point, D and ε resemble to the assessment of the crystallite size and the assessment of the microstrain, individually (Eq. 16 and 17). Through potting 4 sinθ, the extension of the Y-intercept, as well as the slope of the lines, can be used to determine the usual size of the crystallites as well as the strain.

$$D = \frac{K\lambda}{\text{Y Intercept}} \quad (16)$$

$$\varepsilon = \text{Slope} \quad (17)$$

The quantity of dislocations in a unit of volume of a crystalline material (Fe_3O_4@ZIF-8) is measured by the lattice distortion. The crystal's dislocation lines' length is in millimeters per cubic millimeter (m/m^3) Edge displacement Strain energy is produced when a screw distorts a

crystalline structure, creating elastic tension along the dislocation line. Dislocations must be eliminated for maximum strength (Eq. 18):

$$\delta = \frac{1}{D^2} \tag{18}$$

wherever D is the normal crystallite size in nm so it is in unit $1/nm^2$ so the dislocation of Fe_3O_4@ZIF-8 was $4.7x10^{-6}$.

Analysis by the Fourier transform infrared (FTIR) technique

Bands of absorption in Fe_3O_4, ZIF-8, and Fe_3O_4@ZIF-8 were evaluated between 4000 and 400 cm^{-1} infrared spectroscopy. Absorption bands detected for Fe_3O_4 at 2977 cm^{-1} reveal the O-H stretch [27]. Dispersed high peak includes the Fe-O bond absorption at 614 cm^{-1}. The 2500-3500 cm^{-1} band in the ZIF-8 corresponds to the stretching vibrations of the ZIF-8 couples, 1384 cm^{-1} to (C-N) vibration, and 1667 cm^{-1} and 1580 cm^{-1} bend and stretches N-H vibrations in the imidazole, respectively. The 1350-1500 cm^{-1} band, contrasted with, is linked to the complete stretching ring. In particular, the peak of 421 cm^{-1} is derived from the Zn-N method of expansion. Fe_3O_4@ZIF-8 FT-IR spectra were strikingly comparable to ZIF-8 FT-IR spectra, through the exclusion of the peak at 614 cm^{-1} (which can be found in Fe-O bonds). The above investigation indicates that the composite was successfully fabricated [28].

Brunauer-Emmett-Teller (BET)

A porous material's properties and ease of processing for different uses are significantly influenced by the size and volume of its pores. Therefore, it is crucial to know the size and contact area of the pores in a porous layer. Most frequently, the outer layer of the material is determined using the Brunauer-Emmett-Teller technique (BET). A physisorption-reliant on adsorption isotherm is used in BET calculations and a gas's propensity of becoming loosely bound once it originates into interaction with the external of a substance since physisorption is a reversible procedure, a gas can rapidly adsorb and desorb to the content's surface. To find the adsorption isotherm, the quantity of gas adsorption is determined at many different pressures and set temperatures. Liquid nitrogen is used to maintain the temperature, which is currently 77 degrees Celsius. The histogram of the adsorption isotherm displays the total volume of gas adsorbed at various pressures. The curve procedure on the graph represents the type of pores present in the material (Figure 3).

The type I isotherm of Fe_3O_4@ZIF-8 adsorption is the type I isotherm. At a particularly in-service pressure ($P/P_o > 0.9$), a hysteresis loop is detected owing to the appearance of microporous pores on the external surface staying virtually fully inside the microspores that were formerly loaded with an adsorbate. Fe_3O_4@ZIF-8 had the highest BET surface area 475.3 m^2/g, presuming a cross-sectional part of 16.2 Å for the N_2 particle. When stated as the liquid volume at saturation pressure, the pore diameter on average 2.23 nm and the total volume of the pore is 0.2756 cm^3/g. The micropore part of 478.404 m^2/g and the exterior surface area of 28.795 m^2/g (estimated through the t-plot method) were both beneficial for adsorption [29].

SEM analysis

Scanning electron microscopy (SEM), as the primary instrument for elucidating surface morphology, physical characteristics theory, and Fe_3O_4@ZIF-8, is well-considered. This has been examined using SEM and is appropriate to control the porosity, shape, and appropriate size of the adsorbent of Fe_3O_4@ZIF-8. The average size of the nanoparticles, 48 nm, was confirmed by the SEM investigation as being Fe_3O_4@ZIF-8. It has big pores, and all these pores have an incurring high adsorption hood for dye trapping [23].

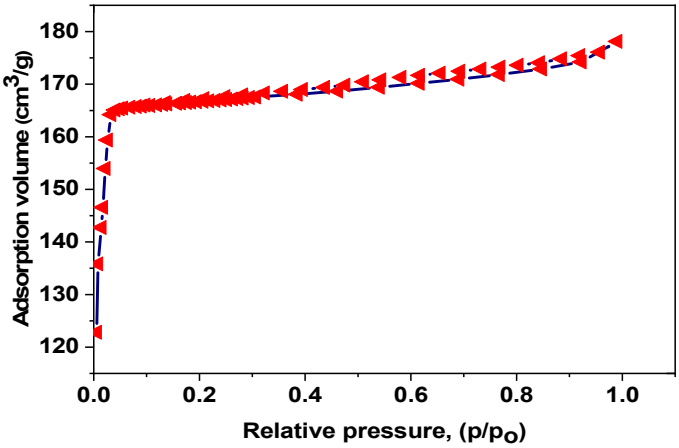

Figure 3. N_2 sorption isotherm of Fe_3O_4@ZIF-8.

Modeling of adsorption isotherms

For the development and operational supervision of an adsorption system, the linking of equilibrium information to theoretical values is a required approach. To elucidate the RB matching experimental information on Fe_3O_4@ZIF-8 adsorbents, two models were adopted. Both of which are based on a statistical physics technique. Two alternative monolayer adsorption methods are the monolayer adsorption model in cumulative impact with the ideal gas technique (MMIG) and the monolayer adsorption model in combination through real gas (MMRG) (MMRG). Experimental adsorption isotherms were modeled exploitation of the MMIG and MMRG models (Figure 4). It's worth mentioning that the RB adsorption potential of all the adsorbents tested increases as the temperature rises [30, 31]. In respect of the concepts utilized, it can be demonstrated that they both closely match the experimental results. As a result, the model's evaluation. As was universally acknowledged, the extent of the correlations R^2 was utilized to control the optimum fit. MMRG model is used to match experimental results that yielded the highest R^2 values. In any case, the fitting precision differences provided by examined models are fairly small, suggesting that the examined systems' gas behavior is far from ideal [32]. the result, physical importance, and basic hypotheses led to the selection of MMRG as one of the most appropriate predictions. Because RB molecules can attract or repel molecules nearby, adsorbate-adsorbate interactions are essential to consider. These RB- Fe_3O_4@ZIF-8 contacts can live together and decide on an adsorption competition that influences the chemistry of RB and Fe_3O_4@ZIF-8 surfaces, depending on the RB and Fe_3O_4@ZIF-8 surface chemistry [26].

Characterization of statistical physics

Mathematical modeling of gas or liquid phase adsorption isotherms using a statistical physics technique is a potential method for spotting surface events throughout adsorption. To gain a deeper grasp of the observed adsorption events, recovered model parameters are given a physical significance (Table 5). As a result, Table 5 contains the recoverable fit variables for the MMIG and MMRG systems. The actuating is investigated and described in this paragraph. Table 5 shows that the number of molecules that have been adsorbed in the pre-position, n, is much less than the unit for Fe_3O_4@ ZIF-8 at all temperatures examined. In terms of the adsorbent surface, this demonstrates that RB can be adsorbed with parallel orientation. Because of the electrostatic attraction between dye cations of nitrogen atoms, we may extrapolate that RB could conceivably

be adsorbed at several active sites on the ZIF-8 surface Van der Waals forces and hydrogen bonding when comes to thermal therapy. As the energy of the surface grew, an agglomeration phenomenon occurred. Furthermore, before or during adsorption, RB molecules clump together in the solution. Temperature affects the density of receptor sites, Nm. While evaluating adsorption temperatures of 30 and 60 degrees Celsius, a greater number of receptor sites show. This is most likely owing to adsorbate desolvation processes and decreased water adsorption, as RB molecules

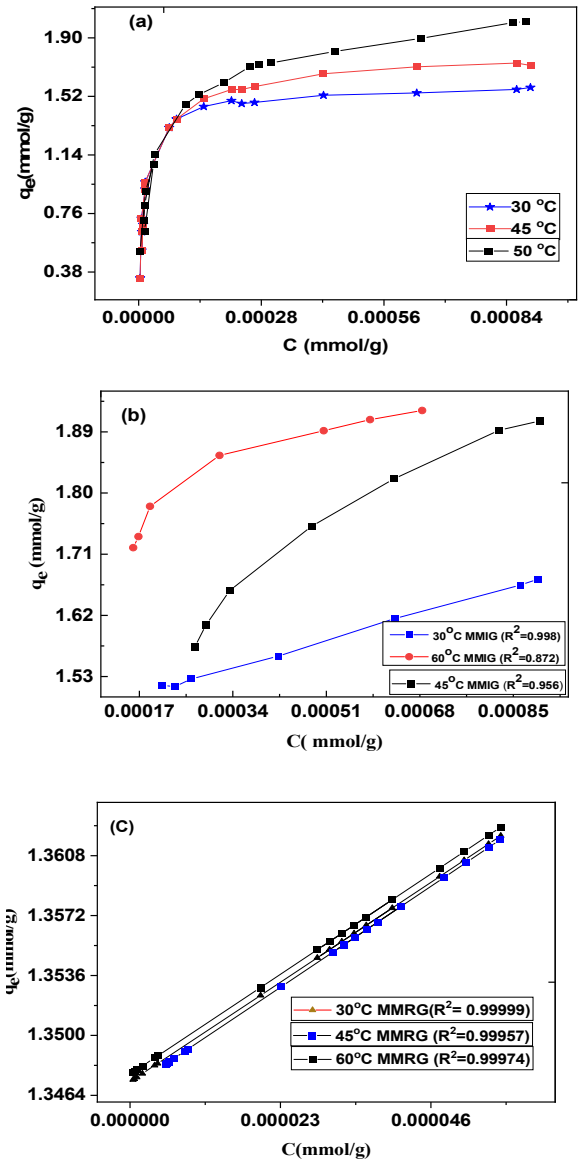

Figure 4. Two variants of the RB experimental adsorption isotherm to Fe_3O_4@ZIF-8 were used to model the isotherm (MMIG and MMRG).

quickly replace it [32]. The greatest adsorption energy (lowest value of w) is found in Fe_3O_4@ ZIF-8, leading to RB full adsorption power. The molecule's volume and molecular pressure cohesion, a and b, respectively. These variables tend to be linked small impact on the systems' adsorption potential. However, there is a slightly greater volume value for RB adsorption at Fe_3O_4@ ZIF-8 at 60 °C, in this condition with the full capacity of adsorption RB. The force of attraction between adsorbed molecules is comparatively diminished (though not eliminated, as explained below) under certain settings, and their reciprocal rivalry is also weakened [26, 30].

The physical significance of parameters

n: The number of adsorbed species per site, expressed as a percentage. This illustrates the adsorbent's surface orientation, as well as the molecules that have been adsorbed throughout the adsorption process. Adsorption ($n > 1$) can be caused by a parallel-oriented multi-anchored method, or by a vertical multimolecular method or a horizontal multimolecular method ($n < 1$).
N_M (mg/g): Sites of receptor concentration: Describes the number of specific receptors that are filled efficiently.
w: Determine the strength of adsorption ($-\Delta Ea$) of RB on Fe_3O_4@ZIF-8 the condition of being liquidated, through the formula below: $-\Delta Ea = RT \ln(w/Cs)$, the concentration of solubility Cs (mg/L) and The ideal gas constant is R (J/K.mol).
a (J.L/mg): Since of the high Fe_3O_4@ZIF-8 and RB contact and low adsorbent-adsorbate contact, a theoretical study displays the development of this parameter; its drop there is a rise in the amount of adsorbed material as well.
b (L/mg): Coolum of molecules: this variable has been proven to evolve in a theoretical investigation; the highest expenditure is accompanied by an increase in the number that has been absorbed. When covolume rate is high, the adsorption energy between RB molecules becomes weak.

Experimental isotherms are adjusted using theoretical models

To identify which statistical physics explanation best fits the real adsorption behavior, we employ computational modeling to correlate the empirical isotherms with both the MMIG and MMRG models. The Levenberg Marquardt algorithm of repetition with a multidimensional non-linear predictor software is the widely used mathematical technique for modifying experimental results with a specific model. To determine which model fits the data the best, three error coefficients are utilized: The R^2 determination coefficient is the first criterion, which assesses the suitability of the fit. The Akaike information criteria is the third, followed by the RMSE (residual root mean square error) (AIC) [28].

The influence of pH

In the adsorption mechanism, pH was among the most crucial variables since it controlled the sorbent's surface charge as well as the composition of the adsorbent solution [17]. The pH (pH_{PZC}) of the surface charge of Fe_3O_4@ZIF-8, wherever the positive surface charge equals the negative surface charge 29. pH_{PZC} of Fe_3O_4@ZIF-8 was discovered to be 4.25. RB is more susceptible to adsorb at $pH > pH_{PZC}$, when the charge on the surface shifts to the negative.

Dye was cationic, so when it was decomposed, it emitted colored dye cations. The amount of color removed reduced when the pH dropped from 8 to 2. The OH^- ion concentration rises at pH 8, and as a result of the OH^- ion absorption, the surface of the Fe_3O_4@ZIF-8 receives a negative charge. Higher dye adsorption may occur at high pH levels as a result of strong electrostatic interaction between the cationic dye molecule and the negatively charged surface of the adsorbent [33]. The quantity of negatively charged ions increases as the pH level increases receptors go up, whereas the amount of positively charged sites falls. Electric force increased adsorption at negatively charged surface areas on the adsorbent surface.

Impact of adsorbent dosage

By varying the adsorbent range, the adsorption of RB to Fe_3O_4@ZIF-8 nanoparticle sorbent was investigated (0.01 to 0.10 g) per 25 mL, RB conc. of $1.51x10^{-3}$ mol/L at 25 ºC and pH 8. The adsorption capacity of RB is shown as a proportion of the adsorbent quantity (Figure 5). As the dose of Fe_3O_4@ZIF-8 is raised, the adsorption capability of RB decreases from 3.73 to 0.376 mmol/g and increases from 0.01 to 0.10 g per 25 mL. As the dosage increases, the Fe_3O_4@ZIF-8 surface area increases while the equilibrium concentration of (RB) decreases [24]. If achieving the mean sorbent load per mass is the objective, a higher quantity of Fe_3O_4@ZIF-8 (0.1 g, 25 mL) and a lower dose (0.01 g, 25 mL) are more suitable.

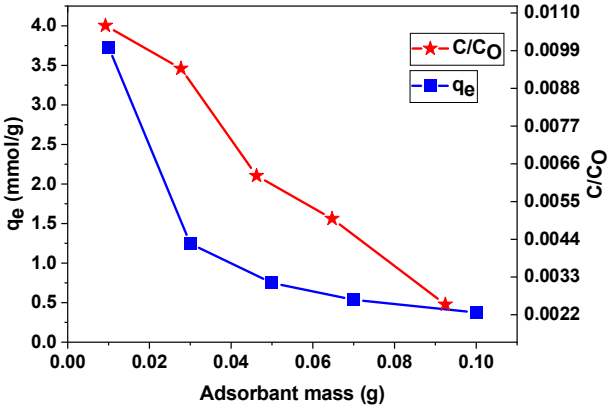

Figure 5. At varied dosages, RB was absorbed by Fe_3O_4@ZIF-8.

Impact of contact time

As well as a dosage of adsorbent 0.02 g, 25 mL of solution capacity, a fullness time of roughly 5-100 min., and a saturation rate of 200 rpm, the impact of the contractual period was evaluated at $1.2x10^{-3}$ mol/L, 25 ºC, and pH 8 for RB, by an adsorbent amount of 0.02 g, 25 mL of solution volume, a capacity time of nearly 5-100 min., besides a saturation rate of the findings demonstrated that colorant adsorption was fast during the primary phases of the adsorption process (60 min) of the adsorbent/adsorbate contact and that the amount percentage elimination was virtually non-existent due to quick adsorption site exhaustion. Efficiency decolorization is initially higher because dye adsorption needs an adsorbent with a larger surface area [34]. Owing to the based on a scale, all of the sites are now colored, and adsorption is slow.

Impact of initial concentration (C_0)

At dye varying concentrations from $6.70x10^{-4}$ to $1.22x10^{-3}$ mol/L at pH 8 and 0.02 g adsorbent doses, the result of the original concentration of the tested dye RB on Fe_3O_4@ZIF-8 was inspected, Later time, it grew to a maximum of 90 min. As the original dye concentration of RB increased, the % removal decreased. The active binding sites of Fe_3O_4@ZIF-8 deteriorated as RB concentrations increased, resulting in a percentage drop in adsorption [35].

Adsorption isotherms

The adsorption of RB on Fe_3O_4@ZIF-8 nanospheres at pH 8 RB at 25 ºC is the isotherm result. Various isothermal models have been utilized to locate aqueous solutions utilizing detailed

isothermal models utilized to explain adsorption procedures, including Langmuir [36], Freundlich [37], Dubinin–Radushkevich [38], and Temkin [39].

Adsorption equilibria isothermal data were investigated using linear isothermal models. Equations and factors for these models' isotherms are listed in Table 2. The Freundlich, Redlich-Peterson, and Temkin isothermal models are analytical formulas for heterogeneous surface multiphase adsorption, while the Langmuir isothermal model replicates a single layer of homogeneous absorption. The R^2 values derived by the Freundlich isothermal model, on the other hand, were higher q_m and K_L are constants are determined using plotting C_e/q_e *vs*. C_e with slope $1/q_m$ and intercept $1/(q_mK_L)$. The separation factor R_L is a constant that has no dimensions, that indicates the key properties of the Langmuir isotherm (Eq. 19) [40, 41]:

$$R_L = \frac{1}{1+c_0K_L} \tag{19}$$

As K_L is the Langmuir constant (mmol/g) and C_0 is the initial adsorbate concentration (mmol/g). When $R_L > 1$, linear when $R_L = 1$, advantageous once $0 < R_L < 1$, and irreversible when $R_L = 0$, R_L amounts suggest that adsorption is unfavorable. The inclusion of the magnetic material, on the other hand, leads the adsorbent to easily break, showing that Fe_3O_4@ZIF-8 has a good probability of adsorbing anionic dyes. Langmuir and Freundlich are identified as the best model to describe the isotherm utilizing Fe_3O_4@ZIF-8 sorbent for RB color adsorption since it is the best fit. The Langmuir model gave RB an $R^2 = 0.9999$ good correlation coefficient.

On the front lines, there's a lot of strength. This isotherm was also considered traditional due to the sorbent's porous nature besides the energy needed in adsorption processes. The sorption energy is 28.7 kJ/mol on average. Regarding the chemisorption method that has been proposed. As per the study, monolayer sorption on a homogeneous surface or even a monolayer on the sorbent surface could be how to dye ion binding occurs. The homogeneous surface hypothesis comforted with the existence the same sort of functional groups (or homogeneous sorption energies).

Table 2. Adsorption isotherms and their linear forms RB onto Fe_3O_4@ZIF-8 [42-44].

Isotherm	Equation	Value of parameters	
Langmuir	$\frac{C_e}{q_e} = \frac{1}{q_mK_L} + \frac{C_e}{q_m}$	$q_{m\ exp}$ (mmol/g)	1.45
		q_m (mmol/g)	1.46
		K_L (L.mmol^{-1})	3.7E+06
		R_L	0.08
Freundlich	$\ln q_e = \ln K_F + \frac{1}{n} \ln C_e$	R^2	0.9999
		n	11.4
		K_F (mmol/g)(L.mmol^{-1})$^{1/n}$	3.602
Dubinin–Radushkevich	$\ln q_e = \ln Q_{DR} - K_{DR}\varepsilon^2$	R^2	0.7048
		Q_{DR}	0.7778
		K_{DR}(J^{2}mol^{-2})	-6.08E-10
		Ea(kJ/mol)	28.7
Temkin	$q_e = \beta_T \ln K_T + \beta_T \ln C_e$	R^2	0.74
		b_T(L/mol)	24114.97
		A_T (kJ/mol)	24.45

Kinetics of adsorption and mechanism studies

Adsorption kinetics study determines the dye absorption, which accurately controls the adsorbate absorption retention time at the RB/Fe_3O_4@ZIF-8 interface. The degree of adsorption of RB was first high, subsequently progressively declined till it arrived at equilibrium, above as the extraction efficiency substantially increased. It was predicted that the maximum adsorption period, likewise

recognized as equilibrium time, was 100 min. The adsorption effectiveness of adsorbents must be evaluated using kinetics experiments. The pseudo-first-order [45] and pseudo-second-order [46, 47], Morris and Weber [48], and Elovich [49] Adsorption kinetic models were used to analyze the method. were utilized in kinetic experiments. Table 3 shows the RB adsorption kinetic parameters for Fe_3O_4@ZIF-8, as well as the equations of kinetic models [49].

Table 3. For the adsorption of RB onto Fe_3O_4@ZIF-8, kinetic parameters, and correlation coefficients [42-44].

Model	Equation	Value of parameters	
Pseudo-First-order kinetic	$\log(q_e - q_t) = \log q_e - \left(\frac{K_1}{2.303}\right) t$	K_1 (min^{-1})	0.0157
		q_e (mmol/g)	0.3838
		R^2	0.822
Pseudo-second-order kinetic	$\frac{t}{q_t} = \frac{1}{K_2 q_e^2} + \frac{t}{q_e}$	K_2 (g $mg^{-1}min^{-1}$)	5.4586
		q_e (mmol/g)	1.49
		R^2	0.9999
Intraparticle diffusion	$q_t = K_i\, t^{1/2} + X$	K_i ($mgg^{-1}min^{1/2}$)	-0.07
		X (mg/g)	0.5579
		R^2	0.1907
Elovich	$q_t = \frac{1}{\beta}\ln(\alpha\beta) + \frac{1}{\beta}\, lnt$	β (g/mg)	-4
		α ($mgg^{-1}.min^{-1}$)	2.75
		R^2	0.3465
Experimental data		q_e (exp) (mmol/g)	1.46

Mechanism of interaction

So because the dye is a cation, when it was decomposed, it produced colored dye cations. When the pH was adjusted from 8 to 2, the amount of color removed decreased. At pH 8, a negatively charged Fe_3O_4@ZIF-8 surface, and a high electrostatic attraction may exist maximum dye adsorption occurs when a negatively charged adsorbent surface interacts with a cationic dye molecule [42]. The adsorption process might Interactions between the positively charged dye ion on the Fe_3O_4@ZIF-8 surface and the negatively charged places can be accounted for. The highly charged adsorbent is more effective in alkaline environments (pH > pHpzc) more generation of OH^-, supported by raised OH^- concentration, resulted in enhanced effectiveness. According to the findings, as a very effective Adsorbent, Fe_3O_4@ZIF-8 can be used to absorb RB.

Active places

The method of analyzing the reactive groups examined RB/Fe_3O_4@ZIF-8 combination with determining the electrophilic/nucleophilic attacking area as well as Molecular electrostatic potential is defined as the electrostatic potential zero regions (MEP). In this study, MEP was utilized to map the complete electron density surface of RB (Figure 6). Different colors were used to indicate the MEP's various values in these maps (red, yellow, green, light blue, and blue). Furthermore, red and yellow hues were utilized to symbolize negative MEP values, which are connected with electrophilic assault. The positive one was blue, which is linked with a nucleophilic attack. The green color characterizes the MEP zero zone in the end. As seen on the MEP map, the MEP of RB discloses that it is most vulnerable to nucleophilic assault (Figure 6) [38].

The density of Electrons Electrostatic potential of molecules (MEP)

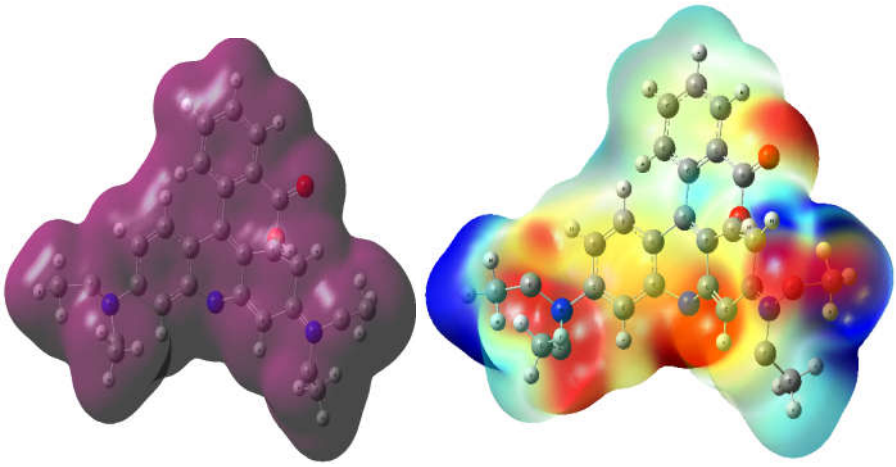

Figure 6. The whole electron density surface was mapped using the electron density molecular electrostatic potential (MEP) for RB.

Thermodynamic parameters

To get insights into adsorption, the thermodynamics of adsorption was determined. Adsorption studies at four different temperatures, the tests were performed: 298, 303, 308, 313, and 318 K. The Gibbs free energy change ΔG^o, the enthalpy change ΔH^o, and the entropy change ΔS^o (Eqs. 20-22):

$$\Delta G^o = -RT \ln K_c \quad (20)$$

$$\Delta G^o = \Delta H^o - T\Delta S^o \quad (21)$$

$$\ln K_C = \frac{-\Delta H^\circ}{RT} + \frac{\Delta S^\circ}{R} \quad (22)$$

As a result, the adsorption period slope and intercept were used to arrive at a result of the ln Kc *vs*. 1/T plot, as well as the intercept of the Arrhenius plot and determination (ΔH^o) and (ΔS^o). The thermodynamic parameters with a positive value (ΔH^o) demonstrate that the mechanism in adsorption methods is endothermic, while (ΔG^o) shows that the reaction is unintentional. The "likelihood" of (ΔG^o) raises as the negativity of (ΔG^o) rises when the temperature rises 45. At increasing temperatures, the RB adsorption reaction on Fe_3O_4@ZIF-8 becomes endothermic with better dye molecule movement and higher adsorbent molecule diffusion rates across Fe_3O_4@ZIF-8 surfaces resulting in improved adsorption efficiency. The rate constant of pseudo-second order was used to confirm dye adsorption [42], and the subsequent relationship of the Arrhenius types (Eq. 23) asserts as a temperature relationship:

$$\ln k_2 = \ln A - E_a/RT \quad (23)$$

Impact of ionic strength

To test the performance of Fe_3O_4@ZIF-8 in real wastewater remediation, the consequence of ionic strength on Fe_3O_4@ZIF-8 effectiveness towards RB was comprehensively simulated using NaCl

levels (10 to 40 g/L; C_0: $1.51x10^{-3}$ mol/L; sorbent dose 0.02 g/25 mL). The concentration of additional opposing (co-interfering) ions present in the aqueous solution has a considerable impact on RB purification. With a slight decrease in Fe_3O_4@ZIF-8 loading capacity, the competitor's density has increased (i.e., Cl^-). The adsorbent's adsorption capacities are still impressive at 1.366 mmol/g (R% = 88.7%) for RB. The slightly noted discrepancy can be explained as follows from a broad perspective. The struggle between negatively charged anionic ions is intensifying (Cl^-) and RB molecules disturbed RB molecules interact with the Fe_3O_4@ZIF-8 adsorbent surface. Furthermore, increasing the concentration of electrolyte counter ions protected the Fe_3O_4@ZIF-8 surface and slowed the adsorption process. Furthermore, as the solution salinity increased, the double electric layer was compressed, resulting in a disgusting force among the RB and the adsorbent surface. Other studies have found that inorganic competitors have antagonistic effects on RB adsorption using diverse adsorbents, which is a more honest description [48].

Other adsorbents in comparison

The performance of this adsorbent was compared to the performance of other adsorbents previously found which indicated that RB can adsorb a lot of Fe_3O_4@ZIF-8.

Desorption studies

Whenever an adsorbent can be used frequently while still performing well in terms of RB removal, separation, and restoration after renewal, this is regarded as cost-effectiveness. Afterward, elution with 0.1-M-HCl solution, the separation (collection) of RB collected by the Fe_3O_4@ZIF-8 adsorbent was investigated. Reusability is a key quality for any porous material, such as MOFs, in terms of practical uses. After three adsorption-desorption cycles, we noticed a shift in Fe_3O_4@ZIF-8 capacity. The most common method for desorption of RB is to modify the pH. Desorption is usually carried out in simple settings. The studied sorbent Fe_3O_4@ZIF-8 was regenerated by carefully washing 0.02 g of the adsorbent in a flask with 0.1 M HCl numerous times until the pH of the washing solution touched 7. Following that, distilled water was used to clean the adsorbent repeatedly. Utilizing ethanol, the remaining colors in the Fe_3O_4@ZIF-8 were eliminated. The clean Fe_3O_4@ZIF-8 was collected and baked for 4 hours at 60 degrees Celsius. The adsorbent was utilized in the following dye adsorption experiment after being regenerated. The adsorbent's renewal effectiveness was discovered to be 98.5% after each adsorption/desorption cycle. The blocking of Fe_3O_4@ZIF-8 adsorption sites is responsible for the slight drop in regeneration effectiveness. The following Eq. (24) was used to compute the regeneration effectiveness:

$$\text{Regeneration efficiency (\%)} = \frac{\text{Amount of desorbed DOX into the elution solution}}{\text{Amount of adsorbed DOX (mmol)}} \times 100 \quad (24)$$

In terms of commercial viability, the discarded adsorbent should be reusable. An alkaline combination of (0.1 M NaOH + 1.2 M NaCl), because of its strong dipole moment, was added to desorb RB dyes from the Fe_3O_4@ZIF-8 surface. The adsorption, desorption, and readsorption cycles were examined for six cycles, and the results are shown in Table 4. They went on to say that the desorbing medium they utilized destabilized the RB@Fe_3O_4@ZIF-8 interaction and then desorbed them from its surface with 98.5% efficiency. Then it was gradually reduced to 92.2% at the 6th cycle. Clearly, this minor decline in the DE% (≈ 6.3%) could be determined from dye molecules clustering (blocking) active sites on the adsorbent surface (chemical reaction). Furthermore, it's worth noting that the Fe_3O_4@ZIF-8 high repeatability determined its economic viability in water and wastewater treatment systems [38].

Table 4. After 6 cycles, the adsorption, desorption, and re-adsorption of RB onto the Fe_3O_4@ZIF-8 adsorbent surface.

Adsorption/desorption cycle	q_e (adsorption) ($mmolg^{-1}$)	q_e (desorption) ($mmolg^{-1}$)	Desorp. (%)
Cycle 1	1.46	1.42	98.5
Cycle 2	1.42	1.408	98.1
Cycle 3	1.408	1.406	95.4
Cycle 4	1.406	1.32	94.7
Cycle 5	1.32	1.282	93.8
Cycle 6	1.282	1.19	92.2

CONCLUSION

In conclusion, Fe_3O_4@ZIF-8 nanoparticles were successfully generated, revealing that the material is an adsorbent with a high adsorption efficiency. The structure of Fe_3O_4@ZIF-8 with an average particle size of 48 nm and an extraordinarily consistent spherical shape. Fe_3O_4@ZIF-8 has a BET surface area of 475 m^2/g and an adsorption pore size of 2.24 nm, which is relatively large. As per the findings, RB adsorption was controlled by the starting initial concentration, pH, contact time, adsorption period, and initial solution temperature. The Langmuir isotherm for RB dye fits the practical data better than the other variations, according to the adsorption equilibrium. RB's mean adsorption energy (E_a) of 28.7 kJ/mol indicates the chemisorption process. The correlation coefficient was used to create a kinetic pseudo-second-order model (R^2). With high efficiency of 1.446 mmol/g, RB was adsorbed at Fe_3O_4@ZIF-8. Adsorption kinetics has been discovered to be flexible. Under experimental conditions, the derived thermodynamic parameters (ΔS^o, ΔH^o and ΔG^o) were determined which represented the spontaneous and endothermic adsorption of RB on Fe_3O_4@ZIF-8 was observed. Fe_3O_4@ZIF-8 has good reusability features due to its high efficiency. After the third run, they are still supplying over 90% of the original capacity, with good magnetic selectivity. Fe_3O_4@ZIF-8 is expected to have a wide range of applications due to its crystalline frameworks, increased surface area, and well-defined standard mesopores.

ACKNOWLEDGMENT

Princess Nourah bint Abdulrahman University Researchers Supporting Project number (PNURSP2022R76), Princess Nourah bint Abdulrahman University, Riyadh, Saudi Arabia.

REFERENCES

1. Martinez-Huitle, C.A.; Rodrigo, M.A.; Sires, I.; Scialdone, O. Single and coupled electrochemical processes and reactors for the abatement of organic water pollutants: A critical review. *Chem. Rev.* **2015**, 115, 13362-13407.
2. El-Bindary, A.A.; El-Sonbati, A.Z.; El-Mosalamy, E.H.; Ahmed, R.M. Potentiometric and conductometric studies on the complexes of some rare earth metals with rhodanine azosulfonamide derivatives, XII. *J. Solution Chem.* **2003**, 32, 617-623.
3. Robinson, T.; Chandran, B.; Nigam, P. Removal of dyes from a synthetic textile dye effluent by biosorption on apple pomace and wheat straw. *Water Res.* **2002**, 36, 2824-2830.
4. Hassan, N.; El-Sonbati, A.Z.; El-Desouky, M.G. Synthesis, characterization, molecular docking and DNA binding studies of Cu(II), Ni(II), Zn(II) and Mn(II) complexes. *J. Mol. Liq.* **2017**, 242, 293-307.
5. Hassan, N.; Shahat, A.; El-Didamony, A.; El-Desouky, M.G., El-Bindary, A.A. Synthesis and characterization of ZnO nanoparticles via zeolitic imidazolate framework-8 and its application for removal of dyes. *J. Mol. Struct.* **2020**, 1210, 28029-28045.

6. El-Desouky, M.G.; El-Bindary, A.A. Magnetic metal-organic framework (Fe_3O_4@ ZIF-8) nanocomposites for adsorption of anionic dyes from wastewater. *Inorg. Nano-Metal Chem.* **2021**, in press. http://doi.org/10.1080/24701556.2021.2007131.
7. El-Sewify, I.M.; Radwan, A.; Shahat, A.; El-Shahat, M.F.; Khalil, M.M.H. Superior adsorption and removal of aquaculture and bio-staining dye from industrial wastewater using microporous nanocubic Zn-MOFs. *Microporous Mesoporous Mater*. **2022**, 329, 111506.
8 Hassan, N.; Shahat, A.; El-Deen, I.M.; El-Afify, M.A.M.; El-Bindary, M.A. Synthesis and characterization of NH_2-MIL-88(Fe) for efficient adsorption of dyes. **2022**, 1258, 132662.
9. El-Sayed, W.N.; Elwakeel, K.Z.; Shahat, A.; Awual, M.R. Investigation of novel nanomaterial for the removal of toxic substances from contaminated water. *RSC Adv.* **2019**, 9, 14167-14175.
10. Kondalkara, M.; Attardea, S.; Fegade, U.; Inamuddin, ??? Altalhi, T.; Ibrahimd, M.M.; Mersal, G.A.M.; Mahmoudd, M.H.H.; Kumeriae, T.; Shahat, A.; El-Bindary, M.A. Experimental and statistical investigation of adsorption mechanism of toxic chromium on Al-Fe-Zn oxide nanocomposite and successful application on industrial wastewater. *Int. J. Environ. Anal. Chem.* **2021**, in press.
11. El-Bindary, A.A.; El-Desouky, M.G.; El-Afify, M.A.M. Thermal and spectroscopic studies of some prepared metal complexes and investigation of their potential anticancer and antiviral drug activity against SARS-CoV-2 by molecular docking simulation. *Biointerface Res. Appl. Chem.* **2021**, 12, 1053-1075.
12. Umemura, A.; Diring, S.; Furukawa, S.; Uehara, H.; Tsuruoka, T.; Kitagawa, S. Morphology design of porous coordination polymer crystals by coordination modulation. *J. Am. Chem. Soc.* **2011**, 133, 15506-15513.
13. Adebisi, S.A.; Amuda, O.S.; Adejumo, A.L.; Olayiwola, A.O.; Farombi, A.G. Equilibrium, kinetic and thermodynamics studies of adsorption of aniline blue from aqueous media using steam-activated carbon prepared from *Delonix regia* pod. *J. Water Res. Protect.* **2015**, 7, 1221-12333.
14. Wu, Y.N.; Li, F.; Zhu, W., Cui, J.; Tao, C.A.; Lin, C.; Hannam, P.M.; Li, G. Metal-organic frameworks with a three-dimensional ordered macroporous structure: Dynamic photonic materials. *J. Angew. Chem. Int. Ed.* **2011**, 50, 12518-12522.
15. Oisaki, K.; Li, Q.; Furukawa, H.; Czaja, A.U.; Yaghi, O.M. A metal-organic framework with covalently bound organometallic complexes. *J. Am. Chem. Soc.* **2010**, 132, 9262-9264.
16. El-Desouky, M.G.; El-Bindary, A.A.; El-Afify, M.A.M.; Hassan, N. Synthesis, characterization, theoretical calculation, DNA binding, molecular docking, anticovid-19 and anticancer chelation studies of some transition metal complexes. *Inorg. Nano-Met. Chem.* **2022**, 52, 1-16.
17. Hassan, N.; Shahat, A.; El-Didamony, A.; El-Desouky, M.G.; El-Bindary, A.A. Mesoporous iron oxide nano spheres for capturing organic dyes from water sources. *J. Mol. Struct.* **2020**, 1217, 128361.
18. Feng, Y.; Li, Y.; Xu, M.; Liu, S.; Yao, J. Fast adsorption of methyl blue on zeolitic imidazolate framework-8 and its adsorption mechanism. *RSC Adv.* **2016**, 6, 109608-109612.
19. Mahmoodi, N.M.; Khorramfar, S.; Najafi, F. Amine-functionalized silica nanoparticle: Preparation, characterization and anionic dye removal ability. *Desalination* **2011**, 279, 61-68.
20. El-Gammal, O.A.; El-Bindary, A.A.; Mohamed, F.Sh.; Rezk, G.N.; El-Bindary, M.A. Synthesis, characterization, design, molecular docking, anti COVID-19 activity, DFT calculations of novel Schiff base with some transition metal complexes. *J. Mol. Liq.* **2022**, 346, 117850.
21. Yahia, M.B.; Yahia, M.B. New insights in the physicochemical investigation of the vitamin B_{12} nucleus using statistical physics treatment: Interpretation of experiments and surface properties. *RSC Adv.* **2020**, 10, 21724-21735.
22. Yahia, M.B.; Aouaini, F.; Yahia, M.B.; Almogait, E.S.; Al-Ghamdi, H. Theoretical investigation of the chlorophyll nucleus adsorption monitored with quartz crystal

microbalance technique: New insights on physicochemical properties. *J. Mol. Liq*. **2019**, 289, 111188.
23. Al-Wasidi, A.S.; AlZahrani, I.IS.; Naglah, A.M.; El-Desouky, M.G.; Khalil, M.A.; El-Bindary, A.A.; El-Bindary, M.A. Effective removal of methylene blue from aqueous solution using metal-organic framework; modelling analysis, statistical physics treatment and DFT calculations. *ChemistrySelect*, **2021**, 6, 11431-11447.
24. Hassan, N.; Shahat, A.; El-Didamony, A.; El-Desouky, M.G.; El-Bindary, A.A. Equilibrium, kinetic and thermodynamic studies of adsorption of cationic dyes from aqueous solution using ZIF-8. *Moroccan J. Chem.* **2020**, 8, 2627-2637.
25. Rafienia, M.; Bigham, A.; Hassanzadeh-Tabrizi, S.A. Solvothermal Synthesis of magnetic spinel ferrites. *J. Med. Sign. Sens.* **2018**, 8, 108-118.
26. Al-Wasidi, A.S.; AlZahrani, I.IS.; Thawibaraka, H.I.; Naglah, A.M.; El-Desouky, M.G.; El-Bindary, M.A. Adsorption studies of carbon dioxide and anionic dye on green adsorbent. *J. Mol. Struct.* **2021**, 1250, 131736.
27. El-Gammal, O.A.; Mohamed, F.Sh.; Rezk, G.N.; El-Bindary, A.A. Structural characterization and biological activity of a new metal complexes based of Schiff base. *J. Mol. Liq.* **2021**, 330, 115522.
28. El-Desouky, M.G.; Abd El-Wahab, M.; El-Bindary, A.A. Interpretations and DFT calculations for polypropylene/cupper oxide nanosphere. *Biointerf. Res. Appl. Chem.* **2021**, 12, 1134-1147.
29. Wurster, D.E.; Oh, E.; Wang, J.C. Determination of the mechanism for the decrease in zinc oxide surface area upon high-temperature drying. *J. Pharm. Sci.* **1995**, 84, 1301-1307.
30. El-Desouky, M.G.; El-Bindary, A.A.; El-Bindary, M.A. Low-temperature adsorption study of carbon dioxide on porous magnetite nanospheres iron oxide. *Biointerface Res. Appl. Chem.* **2021**, 12, 6252-6268.
31. El-Desouky, M.G.; Shahat, A.; El-Bindary, A.A.; El-Bindary, M.A. Description, kinetic and equilibrium studies of the adsorption of carbon dioxide in mesoporous iron oxide nanospheres. *Biointerface Res. Appl. Chem.* **2021**, 12, 3034-3054.
32. Lamine, A.B.; Bouazra, Y. Application of statistical thermodynamics to the olfaction mechanism. *Chem. Senses.* **1997**, 22, 67-75.
33. Özacar, M.; Şengil, İ.A. Adsorption of reactive dyes on calcined alunite from aqueous solutions. *J. Hazard. Mater.* **2003**, 98, 211-224.
34. Ahmad, R.; Kumar, R. Adsorption studies of hazardous malachite green onto treated ginger waste. *J. Environ. Manag.* **2010**, 91, 1032-1038.
35. Sharma, N.; Nandi, B.K. Utilization of sugarcane baggase, an agricultural waste to remove malachite green dye from aqueous solutions. *J. Mater. Environ. Sci.* **2013**, 4, 1052-1065.
36. Langmuir, I. The constitution and fundamental properties of solids and liquids. II. Liquids. *J. Am. Chem. Soc.* **1971**, 39, 1848-1906.
37. Freundlich, H.; Heller, W. The adsorption of *cis*- and *trans*-azobenzene. *J. Am. Chem. Soc.* **1939**, 61, 2228-2230.
38. Dubinin, M.M.; Zaverina, E.D.; Radushkevich, L.V. Sorption and structure of active carbons I. Adsorption of organic vapors. *J. Zhurnal Fizicheskoi Khim.* **1947**, 21, 1351-????.
39. Temkin, M.J.; Pyzhev, V. Recent modifications to Langmuir isotherms. *Acta Physiochim. URSS* **1940**, 40, 217-225.
40. El-Desouky, M.G.; El-Bindary, M.A.; El-Bindary, A.A. Effective adsorptive removal of anionic dyes from aqueous solution. *Vietnam J. Chem.* **2021**, 59, 341-361.
41. El-Bindary, M.A.; El-Desouky, M.G.; El-Bindary, A.A. Metal-organic frameworks encapsulated with an anticancer compound as drug delivery system: Synthesis, characterization, antioxidant, anticancer, antibacterial and molecular docking investigation, *Appl. Organomet. Chem.* **2022**, 36, e6660.

42. El-Bindary, M.A.; El-Desouky, M.G.; El-Bindary, A.A. Adsorption of industrial dye from aqueous solutions onto thermally treated green adsorbent: A complete batch system evaluation. *J. Mol. Liq.* **2021**, 346, 117082.
43. El-Desouky, M.G.; Hassan, N.; Shahat, A.; El-Didamony, A.; El-Bindary, A.A. Synthesis and characterization of porous magnetite nanosphere iron oxide as a novel adsorbent of anionic dyes removal from aqueous solution. *Biointerface Res. Appl. Chem.* **2021**, 11, 13377-13401.
44. El-Desouky, M.G.; Khalil, M.A.; El-Bindary, A.A.; ElBindary, M.A. Biological, biochemical and thermochemical techniques for biofuel production: An updated review. *Biointerface Res. Appl. Chem.* **2022**, 12, 3034-3054.
45. Altalhi, T.A.; Ibrahim, M.M.; Mersal, G.A.; Mahmoud, M.; Kumeria, T.; El-Desouky, M.G.; El-Bindary, A.A.; El-Bindary, M.A. Adsorption of doxorubicin hydrochloride onto thermally treated green adsorbent: Equilibrium, kinetic and thermodynamic studies. *J. Mol. Struct.* **2022**, 1263, 133160.
46. AlHazmi, G.A.A.; AbouMelha, Kh.S.; El-Desouky, M.G.; El-Bindary, A.A. Effective adsorption of doxorubicin hydrochloride on zirconium metal-organic framework: equilibrium, kinetic and thermodynamic studies. *J. Mol. Struct.* **2022**, 1258, 132679.
47. Gubernak, M.; Zapala, W.; Kaczmarski, K. Analysis of amylbenzene adsorption equilibria on an RP-18e chromatographic column. *J. Acta Chromatogr.* **2003**, 13, 38-59.
48. Al-Hazmi, G.A.A.; El-Bindary, M.; El-Desouky, M.G.; El-Bindary, A.A. Efcient adsorptive removal of industrial dye from aqueous solution by synthesized zeolitic imidazolate framework-8 loaded date seed activated carbon and statistical physics modeling. *Desalin. Water Treat.* **2022**, 258, 85-103.
49. Gubernak, M.; Zapala, W.; Tyrpien, K.; Kaczmarski, K. Analysis of amylbenzene adsorption equilibria on different RP-HPLC. *J. Chromatogr. Sci.* **2004**, 42, 457-463.